



# First-principles Prediction of X-Ray Polarization from Magnetic Reconnection in High-frequency BL Lacertae Objects

Haocheng Zhang<sup>1,2</sup> , Xiaocan Li<sup>3</sup> , Dimitrios Giannios<sup>1</sup> , and Fan Guo<sup>2,4</sup> <sup>1</sup> Department of Physics and Astronomy, Purdue University, West Lafayette, IN 47907, USA; [astrophyszhc@hotmail.com](mailto:astrophyszhc@hotmail.com)<sup>2</sup> New Mexico Consortium, Los Alamos, NM 87544, USA<sup>3</sup> Dartmouth College, Hanover, NH 03750, USA<sup>4</sup> Theoretical Division, Los Alamos National Lab, Los Alamos, NM 87545, USA

Received 2020 November 30; revised 2021 March 23; accepted 2021 March 27; published 2021 May 13

## Abstract

Relativistic magnetic reconnection is a potential particle acceleration mechanism for high-frequency BL Lac objects (HBLs). The Imaging X-ray Polarimetry Explorer (IXPE) scheduled to launch in 2021 has the capability to probe the evolution of magnetic field in HBLs, examining the magnetic reconnection scenario for the HBL flares. In this paper, we make the first attempt to self-consistently predict HBL X-ray polarization signatures arising from relativistic magnetic reconnection via combined particle-in-cell and polarized radiation transfer simulations. We find that although the intrinsic optical and X-ray polarization degrees are similar on average, the X-ray polarization is much more variable in both the polarization degree and angle (PD and PA). Given the sensitivity of the IXPE, it may obtain one to a few polarization data points for one flaring event of nearby bright HBLs Mrk 421 and 501. However, it may not fully resolve the highly variable X-ray polarization. Due to temporal depolarization, where the integration of photons with variable polarization states over a finite period of time can lower the detected PD, the measured X-ray PD can be considerably lower than the optical counterpart or even undetectable. The lower X-ray PD than the optical thus can be a characteristic signature of relativistic magnetic reconnection. For very bright flares where the X-ray polarization is well resolved, relativistic magnetic reconnection predicts smooth X-ray PA swings, which originate from large plasmoid mergers in the reconnection region.

*Unified Astronomy Thesaurus concepts:* [Relativistic jets \(1390\)](#); [BL Lacertae objects \(158\)](#); [Computational astronomy \(293\)](#); [Polarimetry \(1278\)](#); [Magnetic fields \(994\)](#); [Blazars \(164\)](#)

## 1. Introduction

High-frequency BL Lacertae objects (HBLs), such as Mrk 421 and 501, are among the most powerful particle accelerators in the universe. They exhibit variable nonthermal-dominated emission up to TeV  $\gamma$ -rays, with the flaring timescale as short as a few minutes in the TeV band, indicating extreme particle acceleration in very localized regions (Albert et al. 2007a, 2007b). Their emission originates from relativistic jets pointing very close to our line of sight. Their spectral energy distribution (SED) has two components: the low-energy component due to synchrotron emission by highly relativistic electrons peaks at soft X-rays, which gives them the name “high-frequency”; the high-energy component extends from X-rays to TeV  $\gamma$ -rays, and is often considered to be Compton scattering by the same electrons that create the synchrotron component (Padovani & Giommi 1995).

Relativistic magnetic reconnection is a candidate particle acceleration mechanism for HBL emission. During this plasma physics process, oppositely directed magnetic field lines break and rejoin, dissipating a large amount of magnetic energy. Recent simulations have suggested that reconnection can efficiently accelerate particles into power-law distributions in a magnetized environment (Guo et al. 2014, 2016; Sironi & Spitkovsky 2014; Werner et al. 2016; Li et al. 2018b, 2019b, and see Guo et al. 2020 for a recent review). Additionally, radiation from relativistic outflows in the reconnection region may experience additional relativistic boosting, making it a very attractive scenario for extreme TeV variability (Giannios et al. 2009; Sironi et al. 2016; Christie et al. 2020). Nevertheless, so far we lack distinct observable signatures

from reconnection that can pinpoint its presence in the HBL emission region.

The scheduled launch of the Imaging X-ray Polarimetry Explorer (IXPE)<sup>5</sup> will open up a unique window to study HBLs via X-ray polarimetry. Recent numerical simulations of reconnection have shown characteristic optical polarization patterns (Zhang et al. 2018, 2020; Hosking & Sironi 2020). If similar patterns exist in the X-ray polarization, the IXPE can unveil the magnetic field structure and its evolution during HBL flares and identify potential reconnection processes. However, the HBL X-ray emission is highly variable. If its polarization is also variable, the integration of photons with different polarization states over time can diminish the detected polarization degree (PD). This “temporal depolarization” must be properly considered in predicting X-ray polarization.

In this paper, we make the first attempt to self-consistently predict the time-dependent X-ray polarization from relativistic magnetic reconnection in HBLs. We use combined particle-in-cell (PIC) and polarized radiation transfer simulations to model the magnetic field and particle evolution from first principles and to include temporal depolarization via ray-tracing. We aim to identify characteristic X-ray polarization patterns from reconnection by comparison with the optical counterpart, which already has rich observational data (Aleksić et al. 2015; Hovatta et al. 2016; Fraija et al. 2017). Section 2 describes the temporal depolarization effect, Section 3 presents our simulation setup and results, and Section 4 discusses implications for optical and X-ray polarimetry.

<sup>5</sup> <https://ixpe.msfc.nasa.gov/>

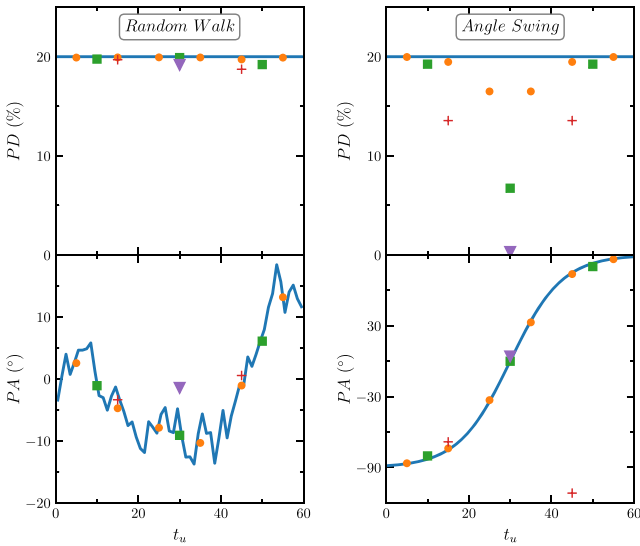


**Figure 1.** Two examples to illustrate the temporal depolarization. The left panels show randomly fluctuating PA, while the right panels show a PA swing event (intrinsic evolution shown by blue curves). The top and bottom panels show the PDs and PAs, respectively. The orange circles, green squares, red crosses, and purple triangles show the detected polarization with different temporal resolution (six, three, two, and one points, respectively).

## 2. Temporal Depolarization

Temporal depolarization can considerably reduce the detected PD by up to 100% with respect to its intrinsic value. This comes from the integration of photons with different polarization states from a variable source over time. Observations have shown that the optical polarization of blazars, including HBLs, can be variable, especially during flares (Blinov et al. 2016; Fraija et al. 2017). This implies magnetic field evolution in the emission region. Therefore, the X-ray polarization, also originating from synchrotron emission, can be variable. X-ray photons carry much more energy than optical ones, even though the X-ray flux is higher than the optical flux for HBLs, so the number of X-ray photons per unit time received by the telescope is much less than the number of optical photons. As a result, the IXPE is unlikely to obtain as high a temporal resolution as the optical polarimeters. The unresolved variations in X-ray polarization then may diminish the detected polarization via temporal depolarization.

We suggest that the temporal depolarization depends on the amplitude of the unresolved variation in polarization angle (PA). Here we illustrate this dependence with two simple examples (Figure 1). Both events have constant flux and  $PD = 20\%$  and last 60 time units  $t_u$ . The first one has randomly fluctuating PA with a maximal change of  $10^\circ$  every  $t_u$ . The second one undergoes a full  $180^\circ$  PA swing from  $-90^\circ$  to  $90^\circ$ . If the two events can only be resolved by a few data points, then the second event generally experiences larger unresolved PA variation per detection. Thus the second event has lower detected PD than the intrinsic one. In particular, if the whole swing is only resolved as one data point, then the detected PD drops to zero; with two points, the PA swing cannot be resolved (Figure 1). For both events, the higher the temporal resolution is, the closer the detected PD and PA can approach the intrinsic value.

The reason lies in the incoherent addition of emission with different polarization states. The detected PD and PA in a

period  $t$  can be calculated from the Stokes parameters (we only consider the linear PD and PA given the synchrotron emission),

$$PD = \frac{\sqrt{\left(\int_0^t Q(t') dt'\right)^2 + \left(\int_0^t U(t') dt'\right)^2}}{\int_0^t I(t') dt'} \quad (1)$$

$$PA = \tan^{-1} \frac{\int_0^t U(t') dt'}{\int_0^t Q(t') dt'}$$

where  $I(t')$ ,  $Q(t')$ , and  $U(t')$  are the intrinsic Stokes parameters at  $t'$ . Since the intrinsic flux and PD are constant for both events, we take  $I = 1$  and  $\sqrt{Q^2 + U^2} = 0.2$  for every  $t_u$ . If the PA fluctuates slightly around  $PA = 0$  as in the first event, then  $Q \lesssim 0.2$  and  $U \sim 0$  at every  $t_u$ . By integrating over  $t$ , the total  $U$  averages to zero, while the total  $Q \sim 0.2t$ . Thus the total PD is still nearly 20% even if the entire event is unresolved. In the second event, the Stokes  $Q$  moves from  $-0.2$  to  $0.2$  then back to  $-0.2$ , while the Stokes  $U$  changes from  $0$  to  $0.2$  then to  $-0.2$  and back to  $0$ . If the temporal resolution is not high enough, especially if the whole event is unresolved, the integrations of  $Q$  and  $U$  are both zero, thus the detected PD is zero. With the high temporal resolution (orange circles in Figure 1), the unresolved PA variation is small per detection, thus the integration does not significantly divert detected PD and PA from intrinsic values. Additionally, since the PA has  $180^\circ$  ambiguity, observations generally consider the PA difference between two consecutive polarization data points to be less than  $90^\circ$ . Therefore, when the time resolution is low (the red cross in Figure 1 lower right), the PA swing is unresolved.

## 3. Optical and X-Ray Polarization from Reconnection

Due to the drastically different radiative cooling of the optical and X-ray emission in HBLs, we expect distinct polarization from these two bands. In this section, we use PIC simulation to self-consistently study the highly dynamical evolution of the magnetic field and nonthermal particles during reconnection (Zhang et al. 2018, 2020), and use ray-tracing polarized radiation transfer to simulate the HBL radiation and polarization signatures (Zhang et al. 2015, 2017), including all time-dependent effects such as the temporal depolarization.

### 3.1. Simulation Setup

We assume a preexisting current sheet in the HBL flaring region. Such structures may exist, for instance, in the striped jet model (Giannios & Uzdensky 2019; Zhang & Giannios 2021). Many HBLs have higher luminosity in the synchrotron spectral component than in the high-energy component, indicating that the cooling by Compton scattering is subdominant (Finke 2013). Since the keV X-ray emission from Mrk 421 and 501 that can be detected by the IXPE is synchrotron, our combined simulations only consider the synchrotron radiation and cooling for simplicity.

The PIC simulation setup is very similar to previous studies (Zhang et al. 2018, 2020; Kilian et al. 2020; Liu et al. 2020). Here we describe some of the key parameters. We perform the 2D PIC simulation in the  $x$ - $z$  plane using the VPIC code

(Bowers et al. 2008). The simulation assumes an electron–ion plasma with realistic mass ratio  $m_i/m_e = 1836$ . The initial particle distributions are Maxwell–Jüttner distributions with uniform density  $n_0$  and temperature  $T_e = T_i = 400m_e c^2$ . This value is generally consistent with the typical low-energy cutoff of the particle spectral distributions based on blazar spectral fitting models (Chen et al. 2011; Ahnen et al. 2018). The upstream thermal electron inertial length is then  $d_e = \sqrt{1 + 3T_e/(2m_e c^2)} d_{e0} \sim 24.5d_{e0}$ . Reconnection starts from a magnetically dominated force-free current sheet,  $\mathbf{B} = B_0 \tanh(z/\lambda) \hat{x} + B_0 \sqrt{\text{sech}^2(z/\lambda) + B_g^2/B_0^2} \hat{y}$ , where  $B_g = 0.2B_0$  is the strength of the guide field, which is the component perpendicular to the antiparallel components  $B_0$ . The half-thickness of the current sheet is  $\lambda = 0.6\sqrt{\sigma_e} d_{e0}$ , where  $d_{e0} = c/\omega_{pe0}$  is the nonrelativistic electron inertial length,  $\omega_{pe0} = \sqrt{4\pi n_e e^2/m_e}$  is the nonrelativistic electron plasma frequency, and  $\sigma_e = B_0^2/(4\pi n_e m_e c^2)$  is the cold electron magnetization parameter (Guo et al. 2014; Sironi & Spitkovsky 2014). We choose  $\sigma_e = 6.4 \times 10^5$ , corresponding to a total magnetization of  $\sigma_0 \approx (m_e/m_i)\sigma_e \approx 350$ . We choose this value so that the upstream electron temperature is much lower than the cold electron magnetization parameter, while the electron spectrum can grow to the typical high-energy spectral cutoff ( $\gamma_{\text{max}} \sim 10^5$  based on spectral fitting models) within a reasonably short period of simulation time. We note that the initial magnetization factor is in the upstream plasma, but the emission region of the reconnection is in the downstream plasma, where the magnetization factor is approximately one. The simulation box size is  $2L \times L$  in the  $x$ – $z$  plane, where  $L = 16,000d_{e0} \sim 653d_e$ . The  $x$ -axis has periodic boundaries for both fields and particles, while the  $z$ -axis has a conductive boundary for fields but reflects particles. The simulation grid size is  $4096 \times 2048$ , with 100 electron–ion pairs in each cell. The cell size  $\Delta x = \Delta z \sim 0.32d_e$  can resolve the upstream electron inertial length. We mimic the synchrotron cooling effect by implementing a radiation reaction force. The strength is set so that the cooling spectral break happens at  $\sim 1$  keV, consistent with observations of Mrk 421 and 501 (Albert et al. 2007a, 2007b).

We use the 3DPOL code to perform polarized radiation transfer simulations (Zhang et al. 2014). This evaluates the polarized synchrotron emission from each cell based on the magnetic field and particle distributions from PIC, then traces the emission to the plane of sky. We fix our line of sight along the  $y$ -axis. We normalize  $B_0$  to 0.1 G and give the simulation domain a bulk Lorentz factor  $\Gamma = 10$  in the  $z$ -direction. These parameters are chosen to be consistent with typical spectral fitting parameters for Mrk 421 and 501 (Błażejowski et al. 2005). The light-crossing time of the simulation box in the  $x$ -direction is  $\tau_{lc} = 32,000t_0$ , where  $t_0 = d_{e0}/c$ . We output the particle and magnetic field from PIC every  $250t_0 \sim 0.0078\tau_{lc}$  to closely follow the evolution of reconnection. We do not include the local Lorentz factor in the radiation transfer because the plasmoid motion is generally nonrelativistic, due to the periodic boundary condition in PIC.

### 3.2. Results

Figures 2 and 3 show the light curve, PD, and PA for the optical and IXPE X-ray bands, respectively; Figures 4 and 5 show snapshots of the particle spatial distribution and polarized emission map during the first X-ray flare (from  $\sim 0.7\tau_{lc}$

to  $\sim 1.0\tau_{lc}$ ) for the two bands. The high magnetization factor and weak guide field lead to very efficient magnetic energy release by magnetic reconnection (Guo et al. 2015; Li et al. 2017, 2018a, 2019a; Liu et al. 2020). After the initial perturbation, the reconnection layer quickly produces a series of plasmoids, which are quasi-circular magnetic structures confining nonthermal particles (Figures 4 and 5, upper panels). Due to the velocity difference, these plasmoids can merge into each other before colliding into the large plasmoid at the periodic boundary. Since the magnetic field lines around the plasmoids are all in the same direction, plasmoid mergers can lead to secondary magnetic reconnection in the contact region. This results in additional particle acceleration in the contact region of merging plasmoids, consistent with the previous findings (Zhang et al. 2018, 2020).

Most importantly, the electrons responsible for optical and X-ray emission suffer from distinct radiative cooling. One can quickly estimate the difference. The synchrotron critical frequency is proportional to  $\gamma_e^2$ , while the cooling time is proportional to  $\gamma_e^{-1}$ . Since the photon energy of the IXPE X-ray band is about 1000 times higher than that of the optical band, the electrons for the X-ray emission cool  $\sim 30$  times faster than those for the optical. This is clearly shown in the light curves (Figures 2 and 3, top panels): the optical light curve keeps rising until  $t \sim 2\tau_{lc}$ , where it starts to cool; but the two X-ray flares both drop to half of the flare peak within  $\sim 0.1\tau_{lc}$ . Because of the strong cooling, the electrons responsible for X-ray emission cannot travel far from their acceleration sites. Figure 5 (upper panels) shows that they are mostly located near the plasmoid center or in the contact region of plasmoid mergers. In contrast, those responsible for optical emission can fill up much larger regions of the reconnection layer (Figure 4). Consequently, the X-ray emission represents the generation of many plasmoids and their mergers, which are very disordered. This leads to the highly variable X-ray light curve and similarly spiky PD and PA for the first flare, where the fast variability originates from small plasmoid mergers. We suggest that the timescales of the fast variability patterns in both flux and polarization during the first X-ray flare are determined by the sizes of the plasmoids. Figure 6 shows snapshots of the X-ray emission maps in this period. We can clearly see that although the simulation box has a periodic boundary in the outflow direction, the high-energy electrons responsible for X-ray emission have barely reached it. The emission is mostly dominated by the central regions of plasmoids in the reconnection layer. By measuring the sizes of these X-ray-emitting regions, we find that they mostly fall in the region between  $0.1L$  and  $0.3L$ , corresponding to  $0.05\tau_{lc}$ – $0.15\tau_{lc}$ . As shown in Figure 3, the timescales match very well with the fast variability patterns in both flux and polarization. We can also see in Figure 5 that during the first X-ray flare, the local polarization vector distributions appear very stochastic without any systematic patterns. This explains the apparently random-walk X-ray PD and PA during the first flare (Figure 3).

The second X-ray flare, however, results from the merging of two large plasmoids. Figures 7 and 8 show the evolution of X-ray and optical polarized emission maps, respectively. As we can see in Figure 8, at  $t \sim 1.6\tau_{lc}$ , a large plasmoid starts to merge into the large plasmoid at the periodic boundary. This merger leads to strong particle acceleration in the contact region, as shown in the snapshot at  $t \sim 1.66\tau_{lc}$ . However, just like the primary reconnection, the newly accelerated particles

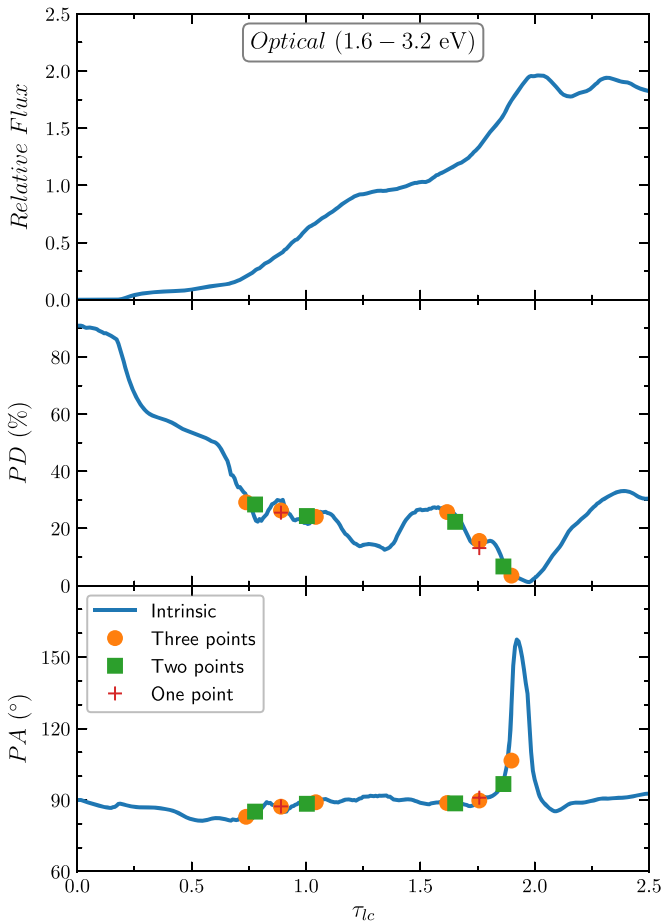


**Figure 2.** From top to bottom are the light curve, PD, and PA for the optical band from our combined simulation. Points represent the detected polarization with various temporal resolutions during the two X-ray flares.

from this secondary reconnection site are not necessarily symmetric in the outflow direction, but there are more particles moving upward than downward. Since the magnetic field lines are quasi-circular in the post-merger plasmoid, the newly accelerated particles will stream along the magnetic field lines, so that the particles going upward will stream clockwise, while those going downward will go counterclockwise. Due to the asymmetry, clockwise motion dominates the radiation signatures, which lights up the magnetic field structure along its trajectory, leading to a smooth PA rotation in the X-ray bands. These results are consistent with Zhang et al. (2018, 2020). One may expect that the large plasmoid merger should lead to a similar PA rotation in the optical band. However, since the electrons responsible for the optical emission cool much more slowly, they occupy a large region of the reconnection layer. As shown in Figure 8, although the plasmoid merger accelerates a large number of electrons, the local polarized flux is much less dominating than the X-ray band. In fact, the polarized flux is nearly symmetrically distributed in the quasi-circular plasmoid. The incoherent addition of the polarized emission thus cancels out the net polarization, making the optical PD drop to nearly zero. In this situation, a tiny excess in a specific direction of the polarized flux can have a huge impact on the net PA, which leads to the large but very narrow spike in the optical PA at  $\sim 2.0\tau_{lc}$ . However, since the optical PD is almost zero, this feature may not be observed. We want to emphasize that the large plasmoid mergers and resulting flare

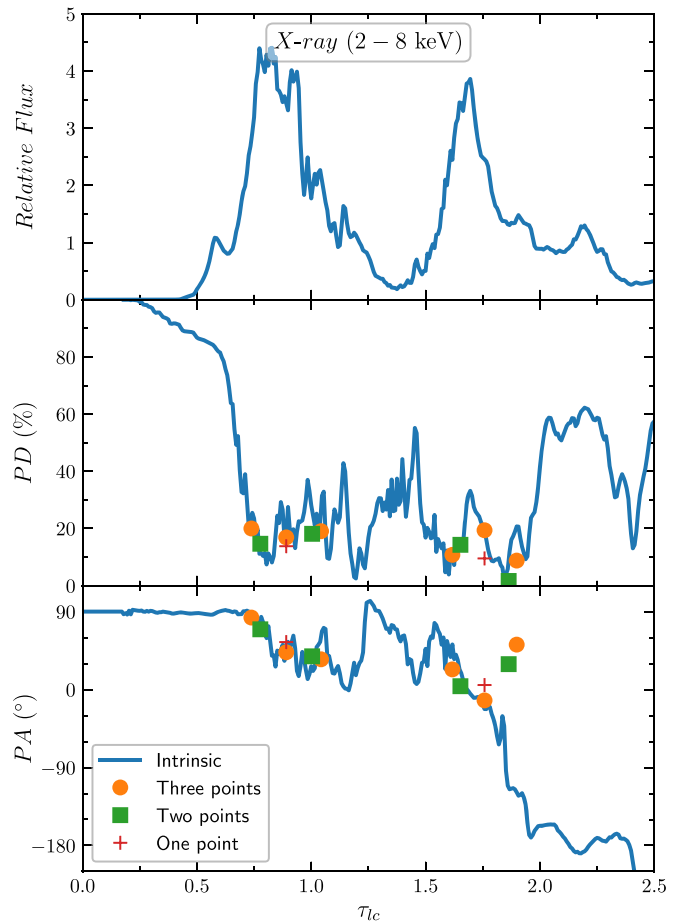


**Figure 3.** Same as Figure 2 but for the IXPE X-ray band.

and PA swings are not always at the periodic boundary. As shown in Zhang et al. (2020), the same can happen between two large plasmoids away from the boundary. Additionally, small plasmoid mergers in the relatively early stage of reconnection may lead to PA swings as well, while large plasmoid mergers do not necessarily lead to asymmetric outflows and PA swings. Nevertheless, our simulation has clearly shown that fast variability in flux and polarization as well as PA swings in the X-ray band can be characteristic signatures for magnetic reconnection in blazars.

The fast polarization variability in X-rays can be hard to resolve. As mentioned above, the temporal depolarization can diminish the detected polarization if the unresolved PA variation is large. To illustrate this effect, here we consider that one X-ray flare in our simulation constitutes the period during which the relative flux is above one. Then the two flares at  $\sim 0.75\tau_{lc}$  and  $\sim 1.7\tau_{lc}$  are of similar duration ( $\sim 0.5\tau_{lc}$ ). We consider three temporal resolutions, where the IXPE can resolve each flare by one, two, and three polarization points, respectively. The detected optical and X-ray PD and PA are shown in Figures 2 and 3 (middle and lower panels). For the first flare, the detected X-ray PD ( $\sim 15\%$ ) is only  $\sim 60\%$  of the optical ( $\sim 25\%$ ) for any resolution. For the second flare, with one X-ray polarization point the PD ( $\sim 9\%$ ) is still about  $\sim 60\%$  of the optical ( $\sim 15\%$ ), but with three points the X-ray PD is comparable to the optical and traces the intrinsic values well. Although three points have not yet resolved the PA rotation (Figure 3, third panel from  $\sim 1.5\tau_{lc}$  to  $\sim 2.0\tau_{lc}$ , and note that the last green and orange PA data points are due to the  $180^\circ$  PA



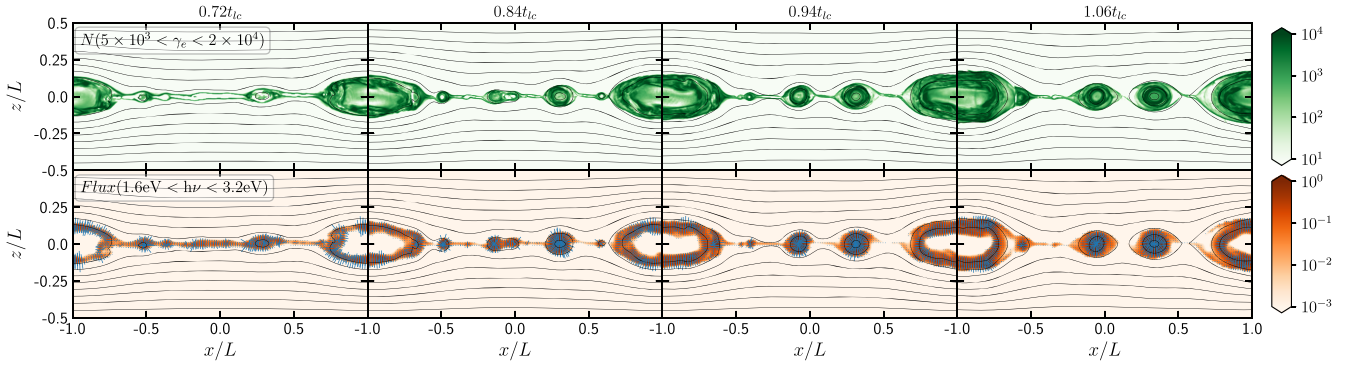


**Figure 4.** From left to right are four snapshots of the particle spatial distribution (upper row) and polarized emission map (lower row) for the optical band during the first X-ray flare. The length and direction of the blue segments in the lower row represent the local polarized flux and angle, respectively.

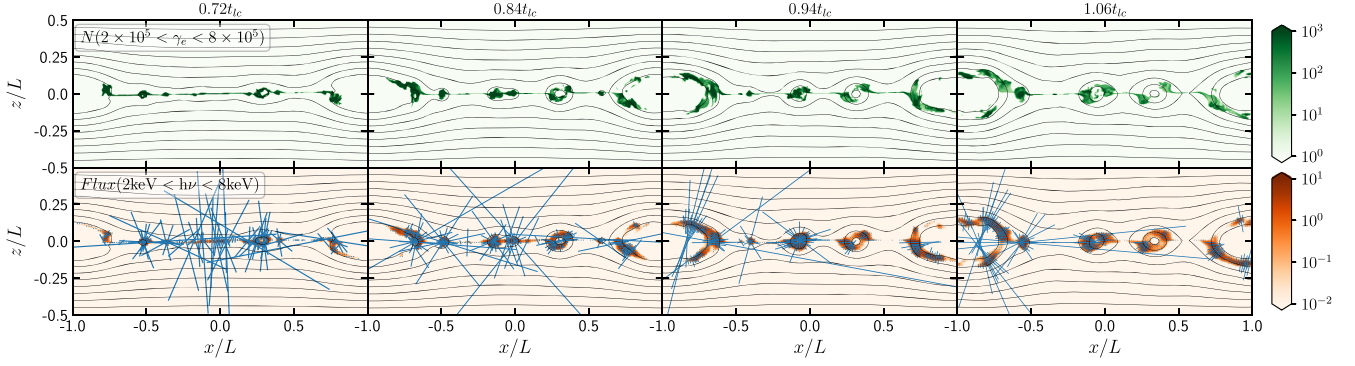


**Figure 5.** Same as Figure 4 but for the X-ray band.

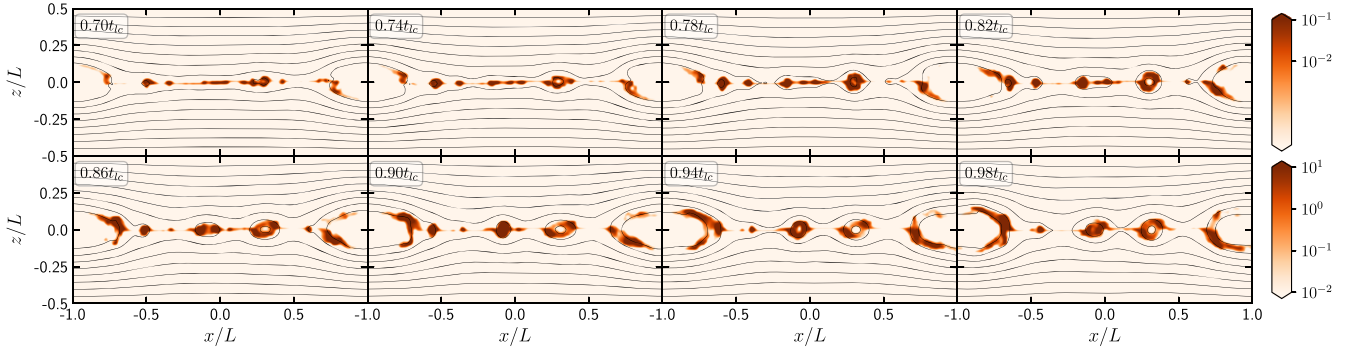


**Figure 6.** Snapshots of the X-ray emission map during the first X-ray flare. The local polarized flux is not plotted so as to better show the size distribution of plasmoids.

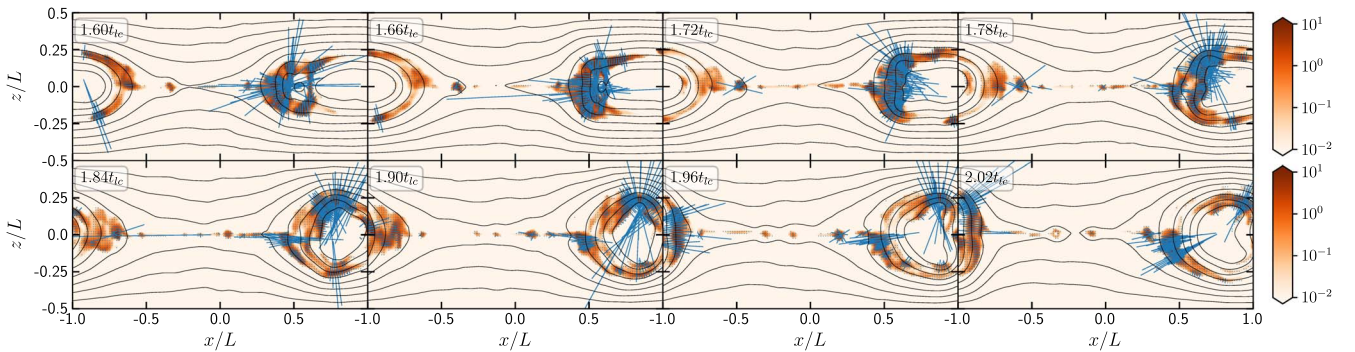


**Figure 7.** Snapshots of the X-ray polarized emission map during the second X-ray flare.

ambiguity), during bright flares the IXPE may have better temporal resolution. The relatively smooth X-ray PA swing can then be a characteristic signature of reconnection.

Figure 9 shows the spectral properties of our simulation. We only plot the snapshots from approximately the start of the first X-ray flare to the end of the second one. We can clearly see that

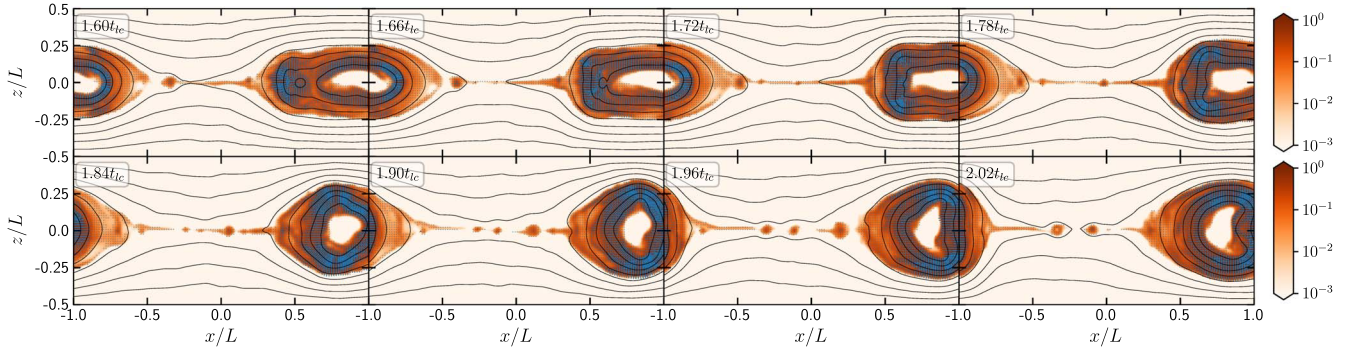


Figure 8. Same as Figure 7 but for the optical band.

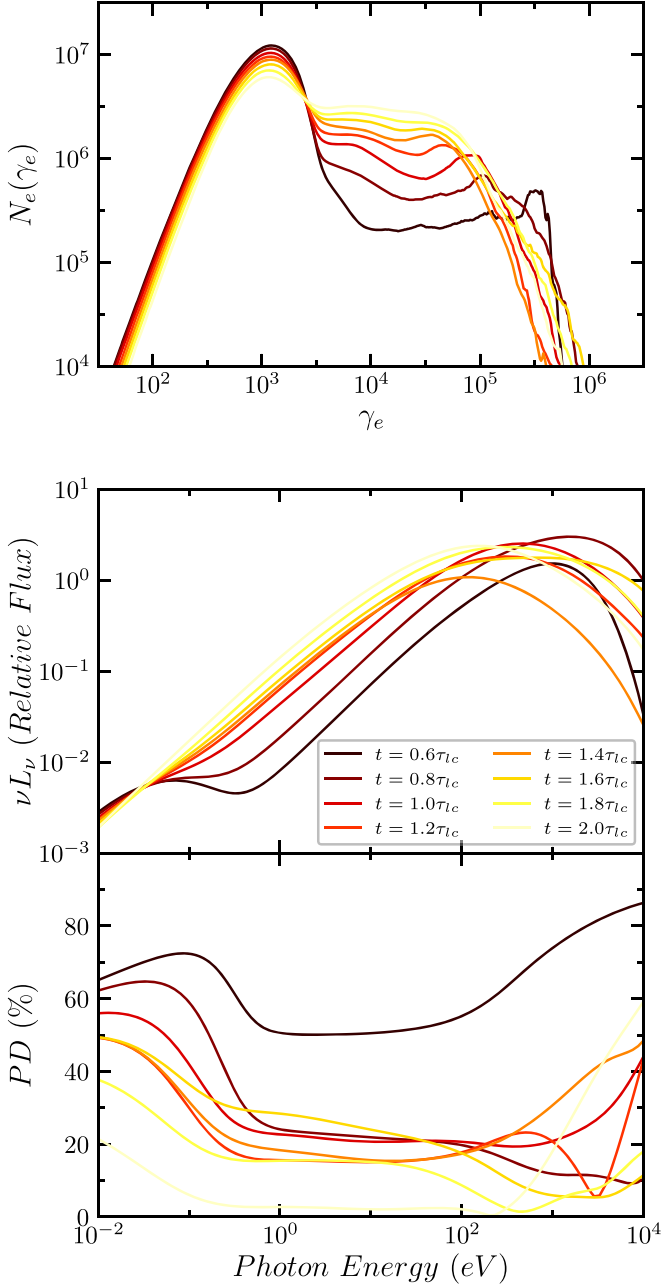


Figure 9. From top to bottom are the snapshots of particle spectra, SEDs of the synchrotron component, and frequency-dependent PDs. SEDs are plotted in relative flux. The particle spectra are in the lab frame of the simulation, while the SEDs and PDs are in the observer’s frame.

the reconnection quickly accelerates electrons so that their spectrum adopts a power-law shape. Since the particle spectrum is very hard from the reconnection, the post-reconnection mean electron Lorentz factor is approximately at the cooling break  $\gamma_c = 10^5$ , although this value can evolve in time due to the dynamical balance between acceleration and cooling. We note that the cooling break here comes from our normalization so that it fits with typical HBL observations, similar to Zhang et al. (2018, 2020). This is through the scale-up of the radiative cooling, and we calculate that the so-called synchrotron burn-off limit is at  $\gamma_b \sim 10^6$  in our simulation (Uzdensky et al. 2011), which is evident from the particle spectrum that cuts off at slightly lower than  $\gamma = 10^6$ . We can see that the synchrotron spectrum is generally harder and extends to higher energies during flare peaks (0.8 to  $1.0\tau_{lc}$  and 1.6 to  $1.8\tau_{lc}$  in the middle panel of Figure 9) than during low states (1.2 to  $1.4\tau_{lc}$ ). Additionally, we can see that the PD variation in optical to UV bands, which is before the cooling break, is much smaller than that in the X-ray bands, which is beyond the cooling break. As mentioned previously, this is due to the radiative cooling, because electrons responsible for X-ray emission only occupy the very active regions in the reconnection layer. All these spectral properties are consistent with our previous findings with flat-spectrum radio quasars (Zhang et al. 2018, 2020).

#### 4. Implication for Observations

To summarize, for the first time we use combined PIC and polarized radiation transfer simulation to study time-dependent optical and X-ray polarization signatures from magnetic reconnection in HBLs. Our study is unique in that we predict polarization signatures from first principles and take into account the often overlooked temporal depolarization effect, which is essential for X-ray polarimetry. We find that the reconnection-driven X-ray light curves show much stronger variability than the optical band, owing to their much faster radiative cooling. Similarly, the intrinsic evolution of the X-ray PD and PA also shows significant microvariability. During X-ray flares, the average intrinsic optical and X-ray PDs are comparable. However, depending on the time resolution of the IXPE data, the detected X-ray PD can be as low as  $\sim 60\%$  of the optical PD in the case of low resolution; in the case of high resolution, the optical and X-ray PDs are comparable, and we may observe X-ray PA swings. These polarization signatures are characteristic of reconnection in HBLs.

Under the magnetic reconnection scenario, the blazar polarization variability of a specific observational band depends on its position in the SED. This results from the

combined effect of radiative cooling and highly dynamical magnetic field evolution (also see Zhang et al. 2020). For observational bands below the synchrotron peak, the cooling of electrons is relatively slow, thus they can fill up plasmoids in the reconnection region. The resulting PD and PA are usually small fluctuations around some mean values, unless there are large plasmoid mergers, where both the PD and PA may experience large changes. On the other hand, the electrons responsible for observational bands near or beyond the synchrotron peak quickly cool after they are accelerated. Therefore, they mostly exist near sites with strong acceleration, such as plasmoid mergers. The resulting polarization signatures thus appear highly variable. Consequently, strongly variable polarization near the synchrotron peak of a blazar can be a signature of the magnetic reconnection. An interesting inference is that observations of optical polarization may expect a “blazar polarization sequence,” where the optical polarization is less variable for higher-frequency blazars. This feature can be tested statistically to identify whether reconnection is the dominant driver of blazar flares.

Another interesting implication is that the temporal depolarization may lower the blazar optical polarization as well. Observations have shown that the optical PD appears lower during PA swings (according to Blinov et al. 2016, Figure 9, the PD during swings is about  $\sim 70\%$  of the average). However, in many flaring events observations can only grab a few data points during the PA swing. As illustrated in Figure 1, the temporal depolarization by itself can lead to this reduction in polarization. Therefore, we need high-cadence optical polarization monitoring to test whether the reduction in polarization during swings is due to a more disordered magnetic field or merely temporal depolarization.





We want to mention a few caveats in our simulations. Our simulations start with a preexisting current sheet, which may only represent one emission region for one flaring epoch. In reality, Mrk 421 and 501 are fairly bright in X-ray bands even during low states (Fraija et al. 2017). This indicates additional emission regions in the jet that are not simulated in our work. Such extra emission regions may contribute to a “quiescent” flux level, so that the flare amplitude shown in our simulations may be lower. Additionally, the quiescent flux may also contaminate the observed polarization signatures. Optical polarimetry often detects  $\lesssim 10\%$  PD for both flaring and quiescent states (Hovatta et al. 2016; Fraija et al. 2017). In our simulations, however, we see  $\sim 20\%$  optical PD. This is because the 2D PIC simulation cannot fully capture turbulence in the reconnection region. Li et al. (2019b) and Guo et al. (2020) have shown that turbulence is very strong in 3D reconnection simulations. This can lead to further reduction in both optical and X-ray polarization. Given a flaring event with  $\sim 10\%$  optical polarization, the detected X-ray polarization considering the temporal depolarization may be as low as  $\sim 5\%$ . Consider the flux of Mrk 421 at  $10^{-10}$  erg cm $^{-2}$  s $^{-1}$  in the 2–8 keV band with a photon index of 2.5: the IXPE will take about 100 ks to obtain a minimal detectable polarization of  $\sim 4\%$ .<sup>6</sup> Therefore, if the emissions from Mrk 421 and 501 are driven by magnetic reconnection, the IXPE may report very low X-ray PD or even nondetection when the sources are in the quiescent state. During bright flares, however, IXPE can have much better time resolution. If we assume that the flux of Mrk

421 can reach  $10^{-9}$  erg cm $^{-2}$  s $^{-1}$ , then IXPE can obtain a minimal detectable polarization of  $\sim 4\%$  within 10 ks, which may be able to fully resolve the fast variability in polarization and X-ray PA swing.

Therefore, we suggest that the IXPE has the potential to distinguish the shock, turbulence, and magnetic reconnection scenarios via X-ray polarimetry. The shock scenario predicts very stable X-ray polarization with much higher PD than the optical band, contrary to the reconnection scenario (Tavecchio et al. 2018, 2020). While the frequency-dependent polarization has not been well studied for the turbulence scenario, generally it is unlikely to produce rather smooth PA swings (Marscher 2014; Kiehlmann et al. 2017; Marscher et al. 2017), which come from plasmoid mergers and may be resolved during bright X-ray flares. On the other hand, reconnection predicts very low and stochastic polarization signatures when the source is not very active, but strongly variable flux and polarization, as well as potential X-ray PA swing, during flaring states. These unique signatures can be examined by future IXPE polarimetry.

We thank the anonymous referee for very helpful and constructive reviews. H.Z. and D.G. acknowledge support from the NASA ATP NNX17AG21G, the NSF AST-1910451, the NSF AST-1816136 grants and by Fermi Cycle 12 Guest Investigator Program #121077. The work by H.Z. and X.L. is funded by the National Science Foundation (NSF) grant PHY-1902867 and Department of Energy (DOE) DE-SC0020219 through the NSF/DOE Partnership in Basic Plasma Science and Engineering. F.G. acknowledges support in part from Astrophysics Theory Program, and DOE support through the LDRD program at LANL.

## ORCID iDs

Haocheng Zhang  <https://orcid.org/0000-0001-9826-1759>  
 Xiaocan Li  <https://orcid.org/0000-0001-5278-8029>  
 Dimitrios Giannios  <https://orcid.org/0000-0003-1503-2446>  
 Fan Guo  <https://orcid.org/0000-0003-4315-3755>

## References

- Ahnen, M. L., Ansoldi, S., Antonelli, L. A., et al. 2018, *A&A*, 620, A181  
 Albert, J., Aliu, E., Anderhub, H., et al. 2007a, *ApJ*, 663, 125  
 Albert, J., Aliu, E., Anderhub, H., et al. 2007b, *ApJ*, 669, 862  
 Aleksić, J., Ansoldi, S., Antonelli, L. A., et al. 2015, *A&A*, 578, A22  
 Błażejowski, M., Blaylock, G., Bond, I. H., et al. 2005, *ApJ*, 630, 130  
 Blinov, D., Pavlidou, V., Papadakis, I. E., et al. 2016, *MNRAS*, 457, 2252  
 Bowers, K. J., Albright, B. J., Yin, L., et al. 2008, *PhPI*, 15, 055703  
 Chen, X., Fossati, G., Liang, E. P., et al. 2011, *MNRAS*, 416, 2368  
 Christie, I. M., Petropoulou, M., Sironi, L., et al. 2020, *MNRAS*, 492, 549  
 Finke, J. D. 2013, *ApJ*, 763, 134  
 Fraija, N., Benítez, E., Hiriart, D., et al. 2017, *ApJS*, 232, 7  
 Giannios, D., & Uzdensky, D. A. 2019, *MNRAS*, 484, 1378  
 Giannios, D., Uzdensky, D. A., & Begelman, M. C. 2009, *MNRAS*, 395, L29  
 Guo, F., Li, H., Daughton, W., et al. 2014, *PhRvL*, 113, 155005  
 Guo, F., Li, X., Daughton, W., et al. 2020, arXiv:2008.02743  
 Guo, F., Li, X., Li, H., et al. 2016, *ApJL*, 818, L9  
 Guo, F., Liu, Y.-H., Daughton, W., et al. 2015, *ApJ*, 806, 167  
 Guo, F., Liu, Y.-H., Li, X., et al. 2020, *PhPI*, 27, 080501  
 Hosking, D. N., & Sironi, L. 2020, *ApJL*, 900, L23  
 Hovatta, T., Lindfors, E., Blinov, D., et al. 2016, *A&A*, 596, A78  
 Kiehlmann, S., Blinov, D., Pearson, T. J., et al. 2017, *MNRAS*, 472, 3589  
 Kilian, P., Li, X., Guo, F., et al. 2020, *ApJ*, 899, 151  
 Li, X., Guo, F., Li, H., et al. 2017, *ApJ*, 843, 21  
 Li, X., Guo, F., Li, H., et al. 2018a, *ApJ*, 855, 80  
 Li, X., Guo, F., Li, H., et al. 2018b, *ApJ*, 866, 4  
 Li, X., Guo, F., & Li, H. 2019a, *ApJ*, 879, 5

<sup>6</sup> The numbers are based on the IXPE WebPIMMS tool at <https://ixpe.msfc.nasa.gov/cgi-aft/w3pimms/w3pimms.pl>.

- Li, X., Guo, F., Li, H., et al. 2019b, [ApJ](#), **884**, 118
- Liu, Y.-H., Lin, S.-C., Hesse, M., et al. 2020, [ApJL](#), **892**, L13
- Marscher, A., Jorstad, S., & Williamson, K. 2017, [Galax](#), **5**, 63
- Marscher, A. P. 2014, [ApJ](#), **780**, 87
- Padovani, P., & Giommi, P. 1995, [ApJ](#), **444**, 567
- Sironi, L., Giannios, D., & Petropoulou, M. 2016, [MNRAS](#), **462**, 48
- Sironi, L., & Spitkovsky, A. 2014, [ApJL](#), **783**, L21
- Tavecchio, F., Landoni, M., Sironi, L., et al. 2018, [MNRAS](#), **480**, 2872
- Tavecchio, F., Landoni, M., Sironi, L., et al. 2020, [MNRAS](#), **498**, 599
- Uzdensky, D. A., Cerutti, B., & Begelman, M. C. 2011, [ApJL](#), **737**, L40
- Werner, G. R., Uzdensky, D. A., Cerutti, B., et al. 2016, [ApJL](#), **816**, L8
- Zhang, H., Chen, X., & Böttcher, M. 2014, [ApJ](#), **789**, 66
- Zhang, H., Chen, X., Böttcher, M., et al. 2015, [ApJ](#), **804**, 58
- Zhang, H., & Giannios, D. 2021, [MNRAS](#), **502**, 1145
- Zhang, H., Li, H., Guo, F., et al. 2017, [ApJ](#), **835**, 125
- Zhang, H., Li, X., Giannios, D., et al. 2020, [ApJ](#), **901**, 149
- Zhang, H., Li, X., Guo, F., et al. 2018, [ApJL](#), **862**, L25